

Fermion disorder operator at Gross-Neveu and deconfined quantum criticalities

Zi Hong Liu,¹ Weilun Jiang,^{2,3} Bin-Bin Chen,⁴ Junchen Rong,⁵ Meng Cheng,^{6,*} Kai Sun,^{7,†} Zi Yang Meng,^{4,‡} and Fakher F. Assaad^{1,§}

¹*Institut für Theoretische Physik und Astrophysik and Würzburg-Dresden Cluster of Excellence ct.qmat, Universität Würzburg, 97074 Würzburg, Germany*

²*Beijing National Laboratory for Condensed Matter Physics and Institute of Physics, Chinese Academy of Sciences, Beijing 100190, China*

³*School of Physical Sciences, University of Chinese Academy of Sciences, Beijing 100190, China*

⁴*Department of Physics and HKU-UCAS Joint Institute of Theoretical and Computational Physics, The University of Hong Kong, Pokfulam Road, Hong Kong SAR, China*

⁵*Institut des Hautes Études Scientifiques, 91440 Bures-sur-Yvette, France*

⁶*Department of Physics, Yale University, New Haven, CT 06520-8120, USA*

⁷*Department of Physics, University of Michigan, Ann Arbor, Michigan 48109, USA*

(Dated: December 23, 2022)

The fermion disorder operator is shown to reveal the entanglement information in 1D Luttinger liquids and 2D free and interacting Fermi and non-Fermi liquids emerging at quantum critical points (QCP) [1]. Here we study, by means of large-scale quantum Monte Carlo simulation, the scaling behavior of disorder operator in correlated Dirac systems. We first demonstrate the logarithmic scaling behavior of the disorder operator at the Gross-Neveu (GN) chiral Ising and Heisenberg QCPs, where consistent conformal field theory (CFT) content of the GN-QCP in its coefficient is found. Then we study a 2D monopole free deconfined quantum critical point (DQCP) realized between a quantum-spin Hall insulator and a superconductor. Our data point to negative values of the logarithmic coefficients such that the DQCP does not correspond to a unitary CFT. Density matrix renormalization group calculations of the disorder operator on a 1D DQCP model also detect emergent continuous symmetries.

Introduction and Motivation.— Entanglement witnesses can reveal the fundamental organizing principle of many-body systems. The disorder operator [2–5] hinges on symmetry properties of a system, such as spin rotational invariance or charge conservation. Here, a subset M of the system is rotated by an angle θ . For states of matter characterized by a finite length scale, such as a band insulator, this rotation only effects the boundary, and generically an area law is expected. For scale invariant systems logarithmic corrections to the area law reveal critical behavior [1, 6, 7]. Furthermore, sub-leading corrections reflect topological order [8].

The above has an obvious overlap with the entanglement entropy (EE) and related entanglement spectrum (ES) [9–30]. Although in some special cases both the Rényi entropy and the disorder operator produce identical results, both quantities differ. Being symmetry based the disorder operator offers more possibilities such as the detection of emergent symmetries. The aim of this letter is to investigate these possibilities for Dirac systems.

The disorder operator, is an equal-time observable with no need for a replica manifold and is easily accessible to auxiliary field determinantal quantum Monte Carlo (DQMC) simulations [31–33]. For a given system with a $U(1)$ global symmetry, with generator $\hat{Q} = \sum_{i \in V} \hat{n}_i$,

the disorder operator carries out a rotation with angle θ in the entanglement region $M \subset V$, i.e., $X(\theta) = \langle \prod_{i \in M} \exp(i\theta \hat{n}_i) \rangle$, as shown schematically in Fig. 1 (d) and (e).

As mentioned above, the disorder operator and EEs are different quantities, with the former formulated in terms of a global symmetry of the model system and the latter defined without any symmetry considerations. However, their connections from entanglement perspective can be established from two important limits of the disorder operator. The first one is in the small angle limit $\theta \rightarrow 0$, where the disorder operator can be mapped to bipartite fluctuations $-\log |X(\theta)| \propto \theta^2 \langle (\sum_{i \in M} (\hat{n}_i - n))^2 \rangle$ [34]. At the (conformal) QCP, when the boundary of region M is not smooth, the scaling behavior of the disorder operator acquires logarithmic corner correction term [13]

$$\ln |X(\theta)| \sim -al + s(\theta) \ln l + c. \quad (1)$$

While the area law coefficient a is sensitive to the UV physics, the log coefficient $s(\theta)$ is universal and reflects the IR physics. For example, in the small θ limit, $s(\theta)$ is proportional to the central charge in the conformal field theory (CFT) critical point [1, 6, 7].

The second limit is for non-interacting systems [1, 6]. For fermions the disorder operator at special angles maps onto the Rényi EE, for example $S_2 = -2 \log |X(\pi/2)|$ and $S_3 = -\log |X(\frac{2\pi}{3})|$. The general case can be found in [1] and a similar relation holds for the free scalar theory [6].

Beyond the Gaussian limit, one needs to study the disorder operator with numerical simulations. For bo-

* m.cheng@yale.edu

† sunkai@umich.edu

‡ zymeng@hku.hk

§ fakher.assaad@physik.uni-wuerzburg.de

son/spin and topologically ordered systems, it was shown that the log-coefficient reflects the CFT content of the QCP [6, 7] and the remaining constant the topological degeneracy [8]. Of special importance to this paper, is the disorder operator of the 2D JQ spin model [35] for the deconfined QCP (DQCP) [36] where the log-coefficient at $\theta = \pi$ is negative [37]. This finding, together with the similar negative log-coefficient in S_2 [26], suggests that the JQ model realization of the DQCP may not be an unitary CFT (or not a CFT at the first place) [38], and calls to reconsider DQCP related phenomena such as the emergent symmetries [35, 39], dangerously irrelevant operators [40, 41], weakly first order transition [42–44], complex fixed points and walking of scaling dimensions [45–47], multicriticalities [48], etc, and the physical mechanism behind them.

Hence, the question arises if the negative log-coefficient observed at the JQ model realization of DQCP is a generic feature or an artifact of the model. Therefore, it is of importance to measure the disorder operator at other 2D DQCP lattice models and also in 1D systems [49, 50]. The cleanest one present, without any difficulties/ambiguities of the two length scale [40, 41], is the model based on the interacting Dirac fermions [51, 52] with emergent $SO(5)$ symmetry from order parameter measurements, as shown in Fig. 1 (a) and Eq. (2). It is the focus of this paper to compute the disorder operator at this DQCP in large scale DQMC simulations.

Models and numerical settings.— We study the model introduced in Ref. [51] with Hamiltonian

$$H = -t \sum_{\langle ij \rangle} (\hat{c}_i^\dagger \hat{c}_j + \text{h.c.}) - \lambda \sum_{\square} \left(\sum_{\langle\langle i,j \rangle\rangle \in \square} i\nu_{ij} \hat{c}_i^\dagger \sigma \hat{c}_j + \text{H.c.} \right) \quad (2)$$

where $\langle \dots \rangle$ and $\langle\langle \dots \rangle\rangle$ refer to nearest and next nearest neighbors on the honeycomb lattice (as shown in Fig. 1 (d)). The phase diagram has been mapped out with DQMC simulations [51, 52, 55], see Fig. 1 (a). As a function of a single parameter λ (with $t = 1$ as the energy unit), the phase diagram shows a GN-Heisenberg QCP at $\lambda_{c1} = 0.0187(2)$ separating a Dirac semi-metall (DSM) and a quantum spin Hall (QSH) insulator, and a DQCP at $\lambda_{c2} = 0.0332(2)$ separating the QSH and s-wave superconductor (SC). The key difference between Eq. (2) and the JQ model is the absence of monopoles. In the JQ model, the $U(1)$ symmetry is emergent since the lattice breaks it down to \mathbb{Z}_4 . As a consequence, quadruple monopoles are symmetry allowed, and a second length scale at which the \mathbb{Z}_4 symmetry is enhanced to $U(1)$ rotational symmetry obscures the numerical analysis [40]. In the model Eq. (2), the $U(1)$ symmetry corresponds to charge conservation present in the microscopic model. Although the computational complexity of DQMC for Dirac fermion is much higher than that of the stochastic series expansion QMC [35] for the JQ model, order parameter calculations support that $SU(2)$ spin and $U(1)$ charge symmetries are enhanced to an emergent $SO(5)$ symmetry at this DQCP. As we shall see below, we

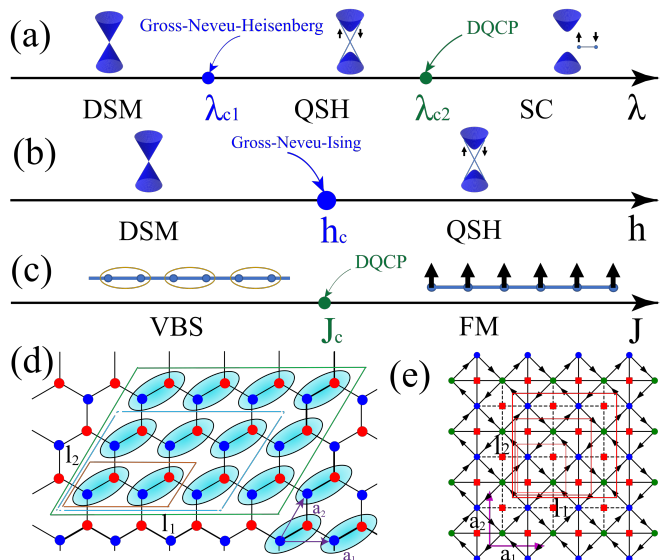


FIG. 1. (a,b,c) Schematic phase diagrams of the 2D DQCP model in Eq. (2), the π -flux model and the 1D DQCP model. The 2D DQCP model has three phases: DSM, QSH, and SC, separated by two QCPs: GN-Heisenberg QCP at λ_{c1} and DQCP at λ_{c2} [51]. For comparison, the π -flux model also possesses DSM and QSH phases, separated by the GN-Ising QCP at h_c [53, 54]. The last one is a 1D model containing VBS and FM phases separated by a DQCP, with $[U(1) \times U(1)] \times \mathbb{Z}_2$ emergent symmetry [49, 50]. (d,e) Sketch of parallelogram entanglement region M in the 2D DQCP model and square entanglement region M in the π -flux model. $\mathbf{a}_1, \mathbf{a}_2$ are unit vectors, and l_1 and l_2 are the linear lengths of M . We define the perimeter $l = 2(l_1 + l_2)$ for both models, which is used to extract the scaling behavior of the disorder operators.

still find the non-unitary signature of the DQCP in this model, similar to that of the JQ model [26, 37]. We also find that the logarithmic corrections of disorder operators appear to violate the emergent $SO(5)$ symmetry.

To probe the $U(1)$ charge and the $SU(2)$ spin symmetries, we consider the disorder operators

$$X_c(\theta) = \left\langle \prod_{i \in M} e^{i\hat{n}_i \theta} \right\rangle, \quad X_s(\theta) = \left\langle \prod_{i \in M} e^{i\hat{m}_i^z \theta} \right\rangle \quad (3)$$

where $\hat{n}_i = \sum_{\sigma} \hat{c}_{i\sigma}^\dagger \hat{c}_{i\sigma}$ and $\hat{m}_i^z = \sum_{\sigma} \sigma \hat{c}_{i\sigma}^\dagger \hat{c}_{i\sigma} = 2\hat{s}_i^z$ are the density and magnetization along the z quantization axis. The operator products \prod are performed in the region M shown in Fig. 1 (d) and (e). From the definitions in Eq. (3), it easily follows that $X_{c/s}(\theta) = X_{c/s}(\theta + 2\pi)$, and $X_c(\pi) = X_s(\pi)$. A more detailed derivation of the disorder operator is presented in Sec.I of the Supplementary Materials (SM) [56]. We use the ALF implementation [57] of the auxiliary field QMC algorithm to study the microscopic model of Eq. (2) and consider linear system sizes $L = 6, 9, 12, 15, 18$ at $\beta = L$.

To further study the GN-QCP and DQCP and for comparisons, we consider two other interacting models. For the GN-QCP, we study Dirac fermions based on the π -flux square lattice with fermion-spin coupling model that

triggers a GN-Ising QCP towards a QSH phase [53, 54]. The phase diagram and the model are shown in Fig. 1 (b) and (e), respectively. The numerical results are shown in the Sec.III in SM [56].

In addition, we consider a 1D DQCP spin model [49, 50] with the Hamiltonian, $H = \sum_i (-J_x S_i^x S_{i+1}^x - J_z S_i^z S_{i+1}^z) + (K_x S_i^x S_{i+2}^x + K_z S_i^z S_{i+2}^z)$, which describes a spin chain containing nearest neighbor ferromagnetic interactions J_x, J_z and next-nearest neighbor antiferromagnetic interactions K_x, K_z . The model possesses a discrete $\mathbb{Z}_2^x \times \mathbb{Z}_2^z$ symmetry. We fix $K_x = K_z = 1/2$ and $J_x = 1$, such that the zero temperature phase diagram is described by only one parameter J_z , shown in Fig. 1 (c). The small/large J_z limits are valence-bond-solid(VBS)/ferromagnetic(FM) phases, separated by a DQCP located at J_c . The emergent symmetry here is $[U(1) \times U(1)] \times \mathbb{Z}_2$. Previous infinite DMRG simulations find $J_c = 1.4645$ [49, 50], and we compute the disorder operator with DMRG to verify the presence of emergent continuous symmetry.

DSM— First, we present the results in the DSM phase of model in Eq. (2). From the measured $|X_c(\theta)|$ and $|X_s(\theta)|$ as a function of the perimeter l (see Sec.II of SM [56]), one can fit the data with the scaling form of Eq. (1), and extract the universal coefficients $s_{c/s}(\theta)$. The results are presented in Figs. 2 (a) and (b). We note that when $\lambda = 0$, there is an exact partial particle-hole symmetry $\hat{c}_\uparrow \rightarrow \hat{c}_\uparrow, \hat{c}_\downarrow \rightarrow \hat{c}_\downarrow^\dagger$, under which $\hat{n}_i \rightarrow \hat{m}_i^\dagger$. It is broken explicitly by the interaction term for $\lambda \neq 0$. Nevertheless, since the interaction is irrelevant in the DSM phase, the symmetry is still present in the IR theory (i.e. it is emergent), and therefore we expect that in the IR $s_s(\theta) = s_c(\theta)$ for all values of the angles throughout the entire DSM phase. The result of the size extrapolation $s_{s/c}(\theta)$ is shown in Fig. 2(g). Within our error bars we have $s_s(\theta) = s_c(\theta)$ and compare well with the free case ($\lambda = 0$). It is known at small angle limit $\theta \rightarrow 0$, $s_{c/s}(\theta)$ satisfies the quadratic form $s_{c/s}(\theta) = \alpha_{c/s} \theta^2$. The IR CFT gives $\alpha_{c/s} = \frac{AN_\sigma C_{J,\text{free}}}{8\pi^2}$, where $N_\sigma = 2$ is the spin flavor, $A \approx 1.30$ is a constant determined by the shape of the region [58] (see SM [56] for more details on A). C_J is the current central charge of the CFT. For the DSM phase we have $C_{J,\text{free}} = 2$ as for free Dirac fermions [59]. Extrapolation of $\alpha_{c/s}$ is shown in Fig. 3 and we obtain, $\alpha_c(\infty) = 0.068(24)$ and $\alpha_s(\infty) = 0.068(31)$, fully consistent with the theoretical expectation $\alpha_{c/s} \approx 0.066$.

QSH, SC— The scaling behavior of the disorder operator in the QSH and SC phases is affected by the gapless Goldstone modes originating from continuous symmetry breaking. Our data for $|X_s(\pi/2)|$ and $|X_c(\pi/2)|$ can be found in Sec. II of the SM [56]. Given our system size we find it challenging to distinguish between additive, $\ln l$, and multiplicative, $\ln \ln l$, logarithmic corrections. The latter is expected for Goldstone modes as observed in the superfluid phase of Boson Hubbard model [7].

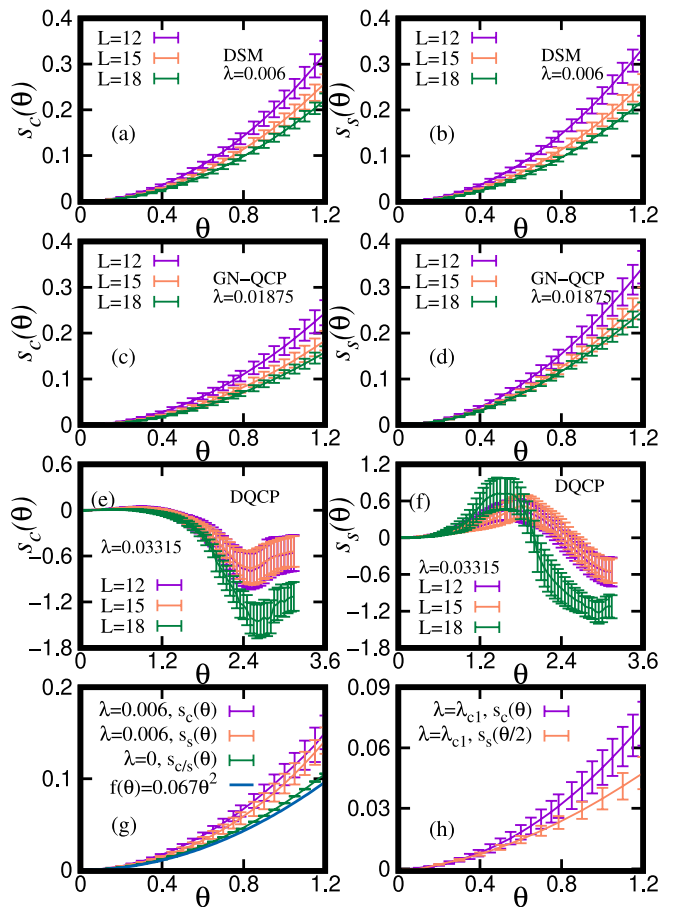


FIG. 2. Logarithmic coefficient $s_{c/s}(\theta)$ in the scaling of the disorder operator as a function of θ in DSM phase (a), (b), at the GN-QCP at λ_{c1} (c), (d) and at the DQCP λ_{c2} (e), (f). Different lines represent different system sizes L . The logarithmic coefficient $s_{c/s}(\theta)$ extrapolated to the thermodynamic limit are presented at (g) in the DSM phase and (h) at GN-Heisenberg QCP.

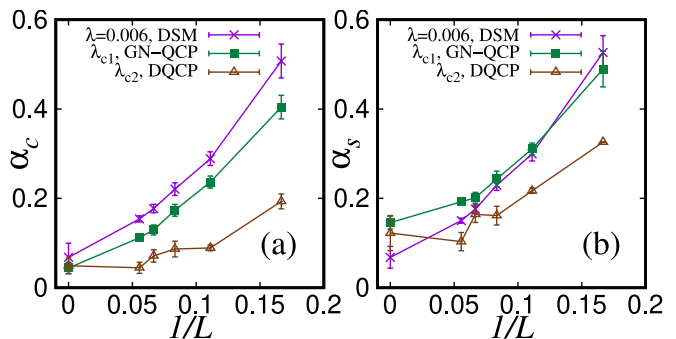


FIG. 3. System-size dependence of $\alpha_{c/s} = s_{c/s}(\theta)/\theta^2$, with $s_{c/s}(\theta)$ obtained from the fitting in Fig. 2. In the DSM phase ($\lambda = 0.006$), extrapolation to the thermodynamic limit $L \rightarrow +\infty$ gives $\alpha_c(\infty) = 0.06(1)$, consistent with the expected CFT value of $\alpha = \frac{AN_\sigma C_{J,\text{free}}}{8\pi^2} \approx 0.066$.

DQCP— There is a body of work suggesting emergent $SO(5)$ symmetry at the DQCP, $\lambda_{c2} = 0.03315$, [41, 60] and it is intriguing to study this from the point of view of the disorder operator. To this aim, our model is unique since the $U(1)$ symmetry is embedded as charge conservation and is present at the UV scale. The conjectured emergent $SO(5)$ symmetry at the DQCP implies that the low energy theory is invariant under $SO(5)$ rotations of the super-spin vector, consisting of the two components of the superconducting order parameter and the three components of the QSH one [61, 62]. Since the charge (spin) disorder operator of Eq. 3 rotates the superconducting (QSH) order parameter by 2θ one expects $s_s(\theta) = s_c(\theta)$ for all values of θ . In the small angle limit this results in $\alpha_s = \alpha_c$ which stands at odds with our results: $\alpha_c(\infty) = 0.049(17)$ and $\alpha_s = 0.12(4)$ albeit with very large error-bars. Furthermore, at larger values of the angle $s_{s/c}(\theta)$ go negative and differ substantially. Negative values of $s_{c/s}(\theta)$ suggests that the DQCP can not be described by a unitary CFT, it is a pseudo-critical point. Similar observations were made in the JQ model, both in the spin disorder operator [37] and entanglement entropy S_2 [26].

GN transitions— In contrast to the DQCP $s_{c/s}(\theta)$ at the GN-Heisenberg transition remains positive in finite systems, as shown in Fig. 2(c), (d), and after extrapolation to the thermodynamic limit, shown in Fig. 2 (h). This confirms the well-established picture that the GN-Heisenberg transition is described by a unitary CFT. For the GN-Ising transition discussed in Sec. III of SM [56] we find that the central charge C_J is slightly reduced compared with that of the free DSM, consistent with the field-theoretical prediction [63].

At the GN-Heisenberg critical point, partial particle-hole symmetry is not present. This is illustrated by the fact that $s_c(\theta) \neq s_s(\theta)$. Interestingly, our data seem to support the relation $s_c(\theta) \simeq s_s(\theta/2)$.

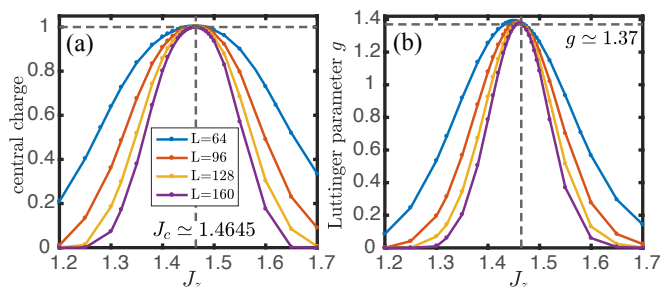


FIG. 4. Emergent symmetry at the 1D DQCP $J_c = 1.4645$. The (a) central charge c and (b) Luttinger parameter g are obtained from the CFT scaling behavior of entanglement entropy $S_{vN} = \frac{c}{3} \ln \tilde{l}$ and disorder operator $-\ln |X_s| = \frac{g}{8} \ln \tilde{l}$, with the conformal distance $\tilde{l} = \frac{L}{\pi} \sin \frac{\pi l}{L}$, which indeed provide the correct values for c and g at the DQCP.

1D DQCP— As a final example, we study the 1D DQCP model [49, 50] of Fig. 1 (c) with DMRG simulations. Our aim is to further confirm that disorder oper-

ators follow the predictions of the IR theory with emergent continuous symmetries. In Ref. [49], the continuous phase transition between ferromagnetic z -FM and VBS phases is determined with high precision. The DQCP point has emergent $[U(1) \times U(1)] \times \mathbb{Z}_2$ symmetry with the x -FM and y -AFM constituting the first $U(1)$, and z -FM and VBS the second. The Luttinger parameter is determined in previous work at the DQCP from two-point correlation functions to be $g = 1.38(1)$ [49]. Since the lattice model only has discrete symmetries, we compute the spin disorder operator defined as $X_s = \langle \prod_{i \in M} \sigma_i^z \rangle$ (corresponding to $\theta = \pi$) for a region M of length l , and extract the scaling behavior from $-\ln(|X_s(l)|) = \frac{g}{8} \ln(l)$, as has been done for the 1d Hubbard model [1] [64]. In Fig. 4(a), the central charge $c = 1$ around the DQCP point $J_z \simeq 1.4645$, is extracted from $S_{vN} = \frac{c}{3} \ln \tilde{l}$ with the conformal distance $\tilde{l} = \frac{L}{\pi} \sin \frac{\pi l}{L}$ and in Fig. 4 (b), the Luttinger parameter $g \simeq 1.37$ is extracted from the disorder operator on the finite-size systems, following the finite-size scaling form $-\ln(X_s(l)) = \frac{g}{8} \ln \tilde{l}$. Away from the critical point, and as supported by the data, the log corrections are expected to vanish since all correlation functions are characterized by a finite length scale.

Discussion.— The disorder operator is a simple quantity to implement in many numerical approaches. Especially in the realm of DQMC and in comparison to EE and ES the disorder operator is very easy to access and can be computed *on the fly*. While, 1D and 2D boson/spin systems as well as nearly free fermion systems have been intensively investigated from the point of view of entanglement, [13–18, 25–30, 65–75], the simplest interacting fermion lattice models in 2D, that is, Dirac fermions and their interaction-driven Gross-Neveu (GN) transitions [51–54, 76–87] remain challenging. This is mainly due to the fact that, the EE, for example the n -th order Rényi entropy S_n , needs to be computed in path-integral QMC simulations with a replicated manifold. Since the typical DQMC simulation for interacting fermions is already very expensive (usually the computational complexity scales as $O(\beta N^3)$ with $\beta = 1/T$ and $N = L^D$) the construction of the replicated manifold and the ensemble average therein [21, 22, 24] is challenging. As a result, small system sizes in 2D and often noisy data is insufficient to extract universal scaling properties in EE. We note recent progress in this regard, with better data quality and the approximate $O(\beta^2 N^3)$ scaling [29].

In contrast no such construction is required for the disorder operator. Logarithmic corrections to the area law capture IR physics and provide invaluable insights into critical points. Although it is challenging to control logarithmic corrections to the area law, especially in DQMC, we have presented a large body of data that shows consistent results for Dirac systems. particular we can test for emergent symmetries at the DSM point by comparing particle-hole related disorder operators. One can also extract the central charge C_J . Emergent symmetries at a 1D DQCP can equally be tested. The CFT constraint on the sign of the coefficient of the logarithmic

correction, $s(\theta) > 0$, allows to test if a putative critical point actually corresponds to a unitary CFT. Using this criterion we were able to show that our realization of a monopole free DQCP does not seem to correspond to a unitary CFT. This is consistent with results for the JQ model [26, 37] and hints to the power of the disorder operator. Given the *simplicity* in computing this quantity, especially within the realm of fermion QMC, many new directions are opened from here, concerning the enigmatic fate of the 2D DQCP theories and their lattice model realizations [35, 39, 42–48, 85, 86].

Acknowledgment.— WLJ, BBC and ZYM acknowledge the support from the Research Grants Council of Hong Kong SAR of China (Grant Nos. 17303019, 17301420, 17301721, AoE/P-701/20 and 17309822), the Strategic Priority Research Program of the Chinese Academy of Sciences (Grant No. XDB33000000), the K. C. Wong Education Foundation (Grant No. GJTD-2020-01), and

the Seed Funding “Quantum-Inspired explainable-AI” at the HKU-TCL Joint Research Centre for Artificial Intelligence. FFA and ZL acknowledge financial support from the DFG through the Würzburg-Dresden Cluster of Excellence on Complexity and Topology in Quantum Matter - *ct.qmat* (EXC 2147, Project No. 390858490) as well as the SFB 1170 on Topological and Correlated Electronics at Surfaces and Interfaces (Project No. 258499086). We thank the HPC2021 platform under the Information Technology Services at the University of Hong Kong, and the Tianhe-II platform at the National Supercomputer Center in Guangzhou for their technical support and generous allocation of CPU time. We equally gratefully acknowledge the Gauss Centre for Supercomputing e.V. (www.gauss-centre.eu) for funding this project by providing computing time on the GCS Supercomputer SuperMUC-NG at Leibniz Supercomputing Centre (www.lrz.de).

-
- [1] W. Jiang, B.-B. Chen, Z. H. Liu, J. Rong, F. F. Assaad, M. Cheng, K. Sun, and Z. Y. Meng, arXiv e-prints , arXiv:2209.07103 (2022).
- [2] L. P. Kadanoff and H. Ceva, Phys. Rev. B **3**, 3918 (1971).
- [3] E. Fradkin, Journal of Statistical Physics **167**, 427 (2017).
- [4] Z. Nussinov and G. Ortiz, Proc. Nat. Acad. Sci. **106**, 16944 (2009).
- [5] Z. Nussinov and G. Ortiz, Annals Phys. **324**, 977 (2009).
- [6] J. Zhao, Z. Yan, M. Cheng, and Z. Y. Meng, Phys. Rev. Research **3**, 033024 (2021).
- [7] Y.-C. Wang, M. Cheng, and Z. Y. Meng, Phys. Rev. B **104**, L081109 (2021).
- [8] B.-B. Chen, H.-H. Tu, Z. Y. Meng, and M. Cheng, Phys. Rev. B **106**, 094415 (2022).
- [9] J. L. Cardy and I. Peschel, Nuclear Physics B **300**, 377 (1988).
- [10] M. Srednicki, Phys Rev Lett **71**, 666 (1993).
- [11] C. Holzhey, F. Larsen, and F. Wilczek, Nuclear Physics B **424**, 443 (1994).
- [12] P. Calabrese and J. Cardy, Journal of Statistical Mechanics: Theory and Experiment **2004**, P06002 (2004).
- [13] E. Fradkin and J. E. Moore, Phys. Rev. Lett. **97**, 050404 (2006).
- [14] H. Casini and M. Huerta, Nucl. Phys. B **764**, 183 (2007).
- [15] A. Kitaev and J. Preskill, Phys. Rev. Lett. **96**, 110404 (2006).
- [16] M. Levin and X.-G. Wen, Phys. Rev. Lett. **96**, 110405 (2006).
- [17] H. Li and F. D. M. Haldane, Phys. Rev. Lett. **101**, 010504 (2008).
- [18] D. Poilblanc, Phys. Rev. Lett. **105**, 077202 (2010).
- [19] H. F. Song, S. Rachel, C. Flindt, I. Klich, N. Laflorencie, and K. Le Hur, Phys. Rev. B **85**, 035409 (2012).
- [20] T. Grover, Physical review letters **111**, 130402 (2013).
- [21] F. F. Assaad, T. C. Lang, and F. Parisen Toldin, Phys. Rev. B **89**, 125121 (2014).
- [22] F. F. Assaad, Physical Review B **91**, 10.1103/PhysRevB.91.125146 (2015).
- [23] N. Laflorencie, Physics Reports **646**, 1 (2016), quantum entanglement in condensed matter systems.
- [24] F. Parisen Toldin and F. F. Assaad, Phys. Rev. Lett. **121**, 200602 (2018).
- [25] J. D’Emidio, Phys. Rev. Lett. **124**, 110602 (2020).
- [26] J. Zhao, Y.-C. Wang, Z. Yan, M. Cheng, and Z. Y. Meng, Phys. Rev. Lett. **128**, 010601 (2022).
- [27] Z. Yan and Z. Y. Meng, arXiv e-prints , arXiv:2112.05886 (2021).
- [28] J. Zhao, B.-B. Chen, Y.-C. Wang, Z. Yan, M. Cheng, and Z. Y. Meng, npj Quantum Materials **7**, 69 (2022).
- [29] J. D’Emidio, R. Orus, N. Laflorencie, and F. de Juan, arXiv e-prints , arXiv:2211.04334 (2022).
- [30] M. Song, J. Zhao, Z. Yan, and Z. Y. Meng, arXiv e-prints , arXiv:2210.10062 (2022).
- [31] R. Blankenbecler, D. J. Scalapino, and R. L. Sugar, Phys. Rev. D **24**, 2278 (1981).
- [32] S. White, D. Scalapino, R. Sugar, E. Loh, J. Gubernatis, and R. Scalettar, Phys. Rev. B **40**, 506 (1989).
- [33] F. Assaad and H. Evertz, in *Computational Many-Particle Physics*, Lecture Notes in Physics, Vol. 739, edited by H. Fehske, R. Schneider, and A. Weiße (Springer, Berlin Heidelberg, 2008) pp. 277–356.
- [34] H. F. Song, S. Rachel, C. Flindt, I. Klich, N. Laflorencie, and K. Le Hur, Phys. Rev. B **85**, 035409 (2012).
- [35] A. W. Sandvik, Phys. Rev. Lett. **98**, 227202 (2007).
- [36] T. Senthil, L. Balents, S. Sachdev, A. Vishwanath, and M. P. A. Fisher, Phys. Rev. B **70**, 144407 (2004).
- [37] Y.-C. Wang, N. Ma, M. Cheng, and Z. Y. Meng, SciPost Physics. **13**, 123 (2022).
- [38] H. Casini and M. Huerta, Journal of High Energy Physics **2012**, 87 (2012).
- [39] N. Ma, Y.-Z. You, and Z. Y. Meng, Phys. Rev. Lett. **122**, 175701 (2019).
- [40] H. Shao, W. Guo, and A. W. Sandvik, Science **352**, 213 (2016).
- [41] A. Nahum, J. T. Chalker, P. Serna, M. Ortuño, and A. M. Somoza, Phys. Rev. X **5**, 041048 (2015).
- [42] A. B. Kuklov, M. Matsumoto, N. V. Prokof’ev, B. V. Svistunov, and M. Troyer, Phys. Rev. Lett. **101**, 050405 (2008).

- [43] K. Chen, Y. Huang, Y. Deng, A. B. Kuklov, N. V. Prokof'ev, and B. V. Svistunov, *Phys. Rev. Lett.* **110**, 185701 (2013).
- [44] J. D'Emidio, A. A. Eberharter, and A. M. Läuchli, arXiv e-prints, arXiv:2106.15462 (2021).
- [45] A. Nahum, *Phys. Rev. B* **102**, 201116 (2020).
- [46] R. Ma and C. Wang, *Phys. Rev. B* **102**, 020407 (2020).
- [47] V. Gorbenko, S. Rychkov, and B. Zan, *Journal of High Energy Physics* **2018**, 108 (2018).
- [48] B. Zhao, J. Takahashi, and A. W. Sandvik, *Phys. Rev. Lett.* **125**, 257204 (2020).
- [49] R.-Z. Huang, D.-C. Lu, Y.-Z. You, Z. Y. Meng, and T. Xiang, *Phys. Rev. B* **100**, 125137 (2019).
- [50] B. Roberts, S. Jiang, and O. I. Motrunich, *Phys. Rev. B* **99**, 165143 (2019).
- [51] Y. Liu, Z. Wang, T. Sato, M. Hohenadler, C. Wang, W. Guo, and F. F. Assaad, *Nature communications* **10**, 1 (2019).
- [52] Y. Liu, Z. Wang, T. Sato, W. Guo, and F. F. Assaad, *Phys. Rev. B* **104**, 035107 (2021).
- [53] Y.-Y. He, X. Y. Xu, K. Sun, F. F. Assaad, Z. Y. Meng, and Z.-Y. Lu, *Phys. Rev. B* **97**, 081110 (2018).
- [54] Y. Liu, W. Wang, K. Sun, and Z. Y. Meng, *Phys. Rev. B* **101**, 064308 (2020).
- [55] M. Bercx, F. Goth, J. S. Hofmann, and F. F. Assaad, *SciPost Phys.* **3**, 013 (2017).
- [56] In this supplemental material, we provide details of QMC simulation, the original data, related theoretical analysis to coordinate with the results in the main text. The supplemental material is organized in four sections: in Section I, we provide the details of the QMC simulation and properties on the disorder operator. Section II, III and IV, we will discuss the results of 2D DQCP model, 2D π -flux model and 1D DQCP model in sequence..
- [57] F. F. Assaad, M. Bercx, F. Goth, A. Götz, J. S. Hofmann, E. Huffman, Z. Liu, F. P. Toldin, J. S. E. Portela, and J. Schwab, *SciPost Phys. Codebases*, 1 (2022).
- [58] X.-C. Wu, C.-M. Jian, and C. Xu, *SciPost Phys.* **11**, 33 (2021).
- [59] J. Helmes, L. E. Hayward Sierens, A. Chandran, W. Witczak-Krempa, and R. G. Melko, *Phys. Rev. B* **94**, 125142 (2016).
- [60] A. Nahum, P. Serna, J. T. Chalker, M. Ortuño, and A. M. Somoza, *Phys. Rev. Lett.* **115**, 267203 (2015).
- [61] A. Tanaka and X. Hu, *Phys. Rev. Lett.* **95**, 036402 (2005).
- [62] T. Senthil and M. P. A. Fisher, *Phys. Rev. B* **74**, 064405 (2006).
- [63] L. Iliesiu, F. Kos, D. Poland, S. S. Pufu, and D. Simmons-Duffin, *Journal of High Energy Physics* **2018**, 36 (2018).
- [64] In our DMRG calculations, we take the periodic boundary condition and confirm the data (including von Neumann EE and disorder operator) are well converged with up to $D = 1024$ bond states kept in the simulations.
- [65] J. Helmes and S. Wessel, *Phys. Rev. B* **89**, 245120 (2014).
- [66] G. Vidal, J. I. Latorre, E. Rico, and A. Kitaev, *Phys. Rev. Lett.* **90**, 227902 (2003).
- [67] M. B. Hastings, I. González, A. B. Kallin, and R. G. Melko, *Phys. Rev. Lett.* **104**, 157201 (2010).
- [68] F. Pollmann, A. M. Turner, E. Berg, and M. Oshikawa, *Phys. Rev. B* **81**, 064439 (2010).
- [69] L. Fidkowski, *Phys. Rev. Lett.* **104**, 130502 (2010).
- [70] S. Humeniuk and T. Roscilde, *Phys. Rev. B* **86**, 235116 (2012).
- [71] S. Inglis and R. G. Melko, *Phys. Rev. E* **87**, 013306 (2013).
- [72] D. J. Luitz, X. Plat, N. Laflorencie, and F. Alet, *Phys. Rev. B* **90**, 125105 (2014).
- [73] S. Inglis and R. G. Melko, *New J. Phys* **15**, 073048 (2013).
- [74] A. B. Kallin, E. M. Stoudenmire, P. Fendley, R. R. P. Singh, and R. G. Melko, *J. Stat. Mech.* **2014**, 06009 (2014).
- [75] A. B. Kallin, K. Hyatt, R. R. P. Singh, and R. G. Melko, *Phys. Rev. Lett.* **110**, 135702 (2013).
- [76] S. Chandrasekharan and A. Li, *Phys. Rev. D* **88**, 021701 (2013).
- [77] Y. Otsuka, S. Yunoki, and S. Sorella, *Physical Review X* **6**, 011029 (2016).
- [78] N. Zerf, L. N. Mihaila, P. Marquard, I. F. Herbut, and M. M. Scherer, *Phys. Rev. D* **96**, 096010 (2017).
- [79] B. Ihrig, L. N. Mihaila, and M. M. Scherer, *Phys. Rev. B* **98**, 125109 (2018).
- [80] T. C. Lang and A. M. Läuchli, *Physical Review Letters* **123**, 137602 (2019).
- [81] M. Schuler, S. Hesselmann, S. Whitsitt, T. C. Lang, S. Wessel, and A. M. Läuchli, *Phys. Rev. B* **103**, 125128 (2021).
- [82] S. M. Tabatabaei, A.-R. Negari, J. Maciejko, and A. Vaezi, *Phys. Rev. Lett.* **128**, 225701 (2022).
- [83] Z. H. Liu, M. Vojta, F. F. Assaad, and L. Janssen, *Phys. Rev. Lett.* **128**, 087201 (2022).
- [84] R. S. Erramilli, L. V. Iliesiu, P. Kravchuk, A. Liu, D. Poland, and D. Simmons-Duffin, arXiv e-prints, arXiv:2210.02492 (2022).
- [85] Y. Da Liao, X. Y. Xu, Z. Y. Meng, and Y. Qi, *Phys. Rev. B* **106**, 075111 (2022).
- [86] Y. Da Liao, X. Y. Xu, Z. Y. Meng, and Y. Qi, *Phys. Rev. B* **106**, 115149 (2022).
- [87] Y. Da Liao, X. Y. Xu, Z. Y. Meng, and Y. Qi, *Phys. Rev. B* **106**, 155159 (2022).

Supplemental Material for

”Fermion disorder operator at Gross-Neveu and deconfined quantum criticalities”

Zi Hong Liu,¹ Weilun Jiang,^{2,3} Bin-Bin Chen,⁴ Junchen Rong,⁵ Meng Cheng,^{6,*} Kai Sun,^{7,†} Zi Yang Meng,^{4,‡} and Fakher F. Assaad^{1,§}

¹*Institut für Theoretische Physik und Astrophysik and Würzburg-Dresden Cluster of Excellence ct.qmat, Universität Würzburg, 97074 Würzburg, Germany*

²*Beijing National Laboratory for Condensed Matter Physics and Institute of Physics, Chinese Academy of Sciences, Beijing 100190, China*

³*School of Physical Sciences, University of Chinese Academy of Sciences, Beijing 100190, China*

⁴*Department of Physics and HKU-UCAS Joint Institute of Theoretical and Computational Physics, The University of Hong Kong, Pokfulam Road, Hong Kong SAR, China*

⁵*Institut des Hautes Études Scientifiques, 91440 Bures-sur-Yvette, France*

⁶*Department of Physics, Yale University, New Haven, CT 06520-8120, USA*

⁷*Department of Physics, University of Michigan, Ann Arbor, Michigan 48109, USA*

(Dated: December 23, 2022)

In this supplemental material, we provide details of simulations, the original data, related theoretical analysis to offer helpful context to coordinate with the main text. The supplemental material is organized as follows: In Section I, we provide the details of the QMC simulations and properties on the disorder operator. In Sections II, III and IV, we will discuss 2d DQCP model, the π -flux model, and 1d DQCP model respectively.

I. QMC SIMULATIONS AND THE DISORDER OPERATOR

A. Quantum Monte Carlo implementation

In this work, we use the ALF [57] implementation of DQMC at finite-temperature. We used a symmetric Suzuki-Trotter decomposition to control the systematic error in observables and adopted an imaginary time step $\Delta\tau t = 0.2$. We set the parameter $t = 1$ and scale the inverse of temperature β as $\beta = L$ in the calculation to access the thermodynamic limit. The coupling strength λ is the parameter we tune in calculation. The disorder operators are defined in parallelogram region in honeycomb lattice as shown in Fig. 1 (c) in the main text.

The measurement of the disorder operator in DQMC can be implemented as [33]

$$\begin{aligned} \langle X(\theta) \rangle &= \left\langle \prod_{i \in M} \exp(i\hat{Q}_i\theta) \right\rangle = \frac{1}{Z} \text{Tr} \left\{ e^{-\beta H} e^{i\hat{c}^\dagger T(\theta)\hat{c}} \right\} \\ &= \sum_{\{s\}} P_s \det(\mathbf{1} + \Delta(\theta)(\mathbf{1} - G_{M,s})) \end{aligned} \quad (\text{S1})$$

for the fermion bilinear local operator \hat{Q}_i , where $G_{M,s}$ is the block Green’s function matrix in subregion M for a given configuration of Hubbard-Stratonovich fields, s . Since the Green function matrix is at hand, the disorder

operator can be computed on the fly without enhancing the computational effort. The matrix elements of $\Delta(\theta) = e^{iT(\theta)} - \mathbf{1}$ dependent on the form of local operator. In our calculation, we consider the local operator to be $\hat{Q}_i = \hat{n}_i$ and $\hat{Q}_i = \hat{m}_i$. If the Hamiltonian we consider is block diagonal in spin basis, we can write down the expression Eq.(S1) as the product of the determinant,

$$\langle X_{c/s}(\theta) \rangle = \sum_{\{s\}} P_s \prod_{\sigma=\uparrow\downarrow} \det\left(\mathbf{1} + \Delta_\sigma^{c/s}(\theta)(\mathbf{1} - G_{A,\sigma})\right) \quad (\text{S2})$$

where $(\Delta_\sigma^c)_{ii' \in M}(\theta) = \delta_{ii'}(e^{i\theta} - 1)$ and $(\Delta_\sigma^s)_{ii' \in M}(\theta) = \delta_{ii'}(e^{i\sigma\theta} - 1)$. For the non-interacting system, $G_{M,s}$ is not dependent on the configuration of Hubbard-Stratonovich fields and the Eq. (S1) reduces to Eq.(S5).

B. Partial particle-hole symmetry

In this part we provide a mapping between the disorder operators $|\langle X_c(\theta) \rangle|$ and $|\langle X_s(\theta) \rangle|$ under partial particle-hole symmetry. We first introduce the definition of the particle-hole symmetry as $P: \hat{c}_{i\uparrow} \rightarrow \hat{c}_{i\uparrow}, \hat{c}_{i\downarrow} \rightarrow (-1)^i \hat{c}_{i\downarrow}^\dagger$. One can easily obtain the follow relation

$$\begin{aligned} P\hat{m}_i P^{-1} &= P \left(\hat{c}_{i\uparrow}^\dagger \hat{c}_{i\uparrow} - \hat{c}_{i\downarrow}^\dagger \hat{c}_{i\downarrow} \right) P^{-1} \\ &= \hat{c}_{i\uparrow}^\dagger \hat{c}_{i\uparrow} - \hat{c}_{i\downarrow} \hat{c}_{i\downarrow}^\dagger = \hat{n}_i - 1 \end{aligned} \quad (\text{S3})$$

We further consider a model hamiltonian with partial particle-hole symmetry such that $P\hat{H}_0 P^{-1} = \hat{H}_0$. Combining with the above equation we have the relation $\langle X_s(\theta) \rangle = e^{-iN_s\theta} \langle X_c(\theta) \rangle$, where N_s represent the total number of site inside the region M . Since the measurement of the disorder operators are based on the absolute

* m.cheng@yale.edu

† sunkai@umich.edu

‡ zymeng@hku.hk

§ fakher.assaad@physik.uni-wuerzburg.de

values $|\langle X_{c/s}(\theta) \rangle|$, the additional phase factor generated by transformation P does not change the result. In summary, the disorder operators $|\langle X_c(\theta) \rangle|$ and $|\langle X_s(\theta) \rangle|$ are the same in the model with partial particle-hole symmetry.

II. 2D DQCP MODEL

First, we focus on the model whose Hamiltonian is introduced in Eq.(1) in the main text. To begin, the mean field limit of the Hamiltonian is discussed. Next, we display our DQMC results. We use the RG invariant quantities to determine λ_{c1} and λ_{c2} , consistent with the results of previous papers. The unprocessed simulation results on the disorder operator and fitting results for α for the interacting case are then provided.

A. Mean field limit

Besides the discussion of the QMC implementation of the disorder operator in the interacting model, in this section, we also provide a simple test by using mean field hamiltonians. For the honeycomb lattice we induced the orders in the phase diagram by including mass terms:

$$H_{\text{MF}} = -t \sum_{\langle ij \rangle \sigma} (\hat{c}_{i\sigma}^\dagger \hat{c}_{j\sigma} + h.c.) + m \sum_{i\sigma} (-1)^i \hat{c}_{i\sigma}^\dagger \hat{c}_{i\sigma} - \lambda \sum_{\square} \mathbf{N} \cdot \left(\sum_{\langle\langle ij \rangle\rangle \in \square} iv_{ij} \hat{c}_i^\dagger \boldsymbol{\sigma} \hat{c}_j + h.c. \right). \quad (\text{S4})$$

Here, m is the staggered mass in real space that generates the charge density wave (CDW) long range order. The mass term of amplitude λ is given by the vector product of the $O(3)$ vector \mathbf{N} and the generalized spin-orbit coupling term, which produces the long-range QSH order. The Hamiltonian of Eq. (S4) only contains fermion bilinear terms and can be solved exactly. For a given fermion bilinear Hamiltonian $H_{\text{bilinear}} = \hat{c}^\dagger K \hat{c}$, the disorder operator can be calculate using the following simple formula

$$\begin{aligned} \langle X_\alpha(\theta) \rangle &= \frac{1}{Z} \text{Tr} \left\{ e^{-\beta H_{\text{bilinear}}} X_\alpha(\theta) \right\} \\ &= \frac{1}{Z} \text{Tr} \left\{ e^{-\beta \hat{c}^\dagger K \hat{c}} e^{i\hat{c}^\dagger T(\theta) \hat{c}} \right\} \\ &= \det \left(G + e^{iT(\theta)} (\mathbf{1} - G) \right) \end{aligned} \quad (\text{S5})$$

where the matrix $T(\theta)$ is a diagonal matrix with nonzero diagonal element when the matrix index belong to the region M and $G = (\mathbf{1} + e^{-\beta K})^{-1}$ is the Green's function. This allows for an efficient calculation of the determinant in Eq. (S5). In the following, we focus on the disorder operator $X_{c/s}(\theta)$ as defined in the main text and discuss their behavior for different mean field Hamiltonians.

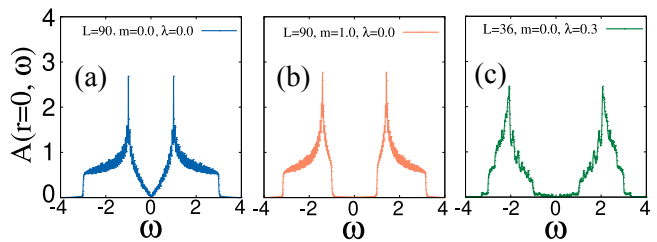


FIG. S1. Local density of state(LDOS) of the model Eq. (S4) with different model parameters. (a) is the free fermion LDOS for the honeycomb lattice with system size $L = 90$. In (b) we consider finite the charge density wave mass by setting $m = 1$ and $\lambda = 0$. In (c) we consider the finite QSH type mass by setting $\lambda = 0.3$ and $m = 0$.

Fig. S1 depicts the local density of states (LDOS) of the model in Eq. (S4) at various mean-field parameters. By setting $t = 1$, $m = 0$ and $\lambda = 0$, Eq. (S4) describe a stable Dirac semi-metal ground state in the thermodynamic limit, as presented in Fig. S1 (a). Without the mass term, the Hamiltonian is block diagonal in the spin basis so that the disorder operator in the charge and spin channels are identical. We calculate the disorder operator with the parallelogram region as in the Fig.1 (c) in the main text. In Fig. S2 (a), for a given rotation angle θ , the disorder operator $X(\theta)$ is dominated by the perimeter law decay, $\ln |X_{c/s}(\theta)| \sim -al + s(\theta) \ln l + c$. As we discussed above, the free Dirac system is a typical conformal fixed point and the disorder operator has sub-leading logarithmic corrections [59, 63]. We fit the data, Fig. S4, to extract the logarithmic coefficient $s(\theta)$ as a function of angle, Fig. S2 (b). Apparently, at small angle, $s(\theta) \sim \alpha\theta^2$. At large system size, the quadratic coefficient α converges to a stable value $\alpha = 0.067(5)$. This is comparable to $\alpha = 0.0658$ obtained in the thermodynamic limit. It is equally consistent with the other free Dirac fermion computation for the π -flux model in Sec. III. Specifically, we obtain the analytic density correlation function combining the corner distribution of the region M , where the detailed analysis is presented in Sec. III D. The slight differences in our results stem from finite size effect, which can be eliminated by extrapolation.

In Fig. S3, we present the disorder operator results for massive Dirac system. In Fig. S3 (b), we set $t = 1$, $m = 1.0$ and $\lambda = 0$, which turns on the staggered CDW mass term that breaks sublattice symmetry. The CDW mass term is diagonal in the spin basis, such that the disorder operators are channel independent. The disorder operator in the massive fermion exhibit a much slower decay than the gapless Dirac fermions, but is still dominated by a perimeter law decay. In Fig. S3(c), we set the parameter $t = 1$, $m = 0$, $|\lambda \mathbf{N}| = 1$ and $N_x = N_y = N_z$ to turn on the QSH mass term. The QSH mass term breaks the $SU(2)$ symmetry of free Dirac fermion which removes the degeneracy of two channels in the disorder operator. Due to the fact that the $SU(2)$ symmetry break into $U(1)$

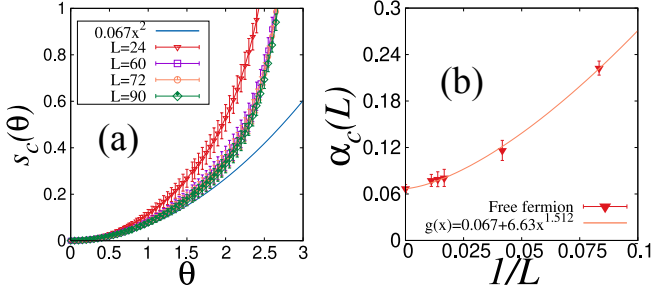


FIG. S2. (a) Logarithmic correction term $s_c(\theta)$ extract from the disorder operator $X_c(\theta)$ by using the numerical fitting as function of rotation angle θ . (b) The quadratic coefficient $\alpha_c(L)$ as function of $1/L$ from free fermion model.

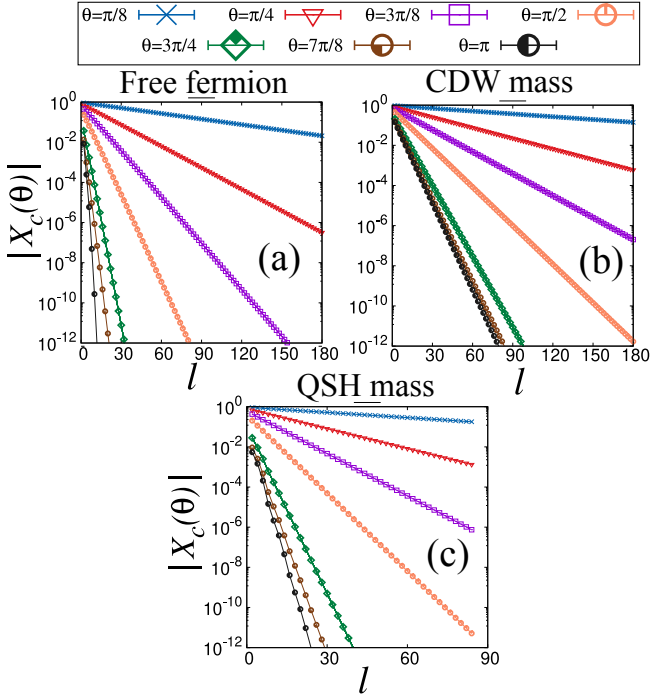


FIG. S3. Disorder operator $X_c(\theta)$ of model Eq.(S4) defined in charge channel as function of perimeter l . We set the y axis in logarithmic scale. In (a) we consider free fermion model in honeycomb lattice by setting $m = \lambda = 0$. In (b) we consider the model with finite CDW mass $m = 1.0$. In (c) we set $\lambda = 0.3$ to observe the effect of QSH type mass term. We choice system size $L = 90$ at (a)(b) and $L = 36$ at (c).

symmetry correspond to the rotation around axis \mathbf{N} in the mean field Hamiltonian, the spin disorder operator $X_s(\theta)$ is not well defined when $\mathbf{N}/|\mathbf{N}| \neq \mathbf{e}_z$. However, the global charge conservation is present for the QSH mass such that $X_c(\theta)$ is still well defined. In Fig. S3(c), the decay rate of $X_c(\theta)$ is dominated by the perimeter law. As apparent from Fig. S4(c) logarithmic corrections to the area law are absent in the massive CDW phase.

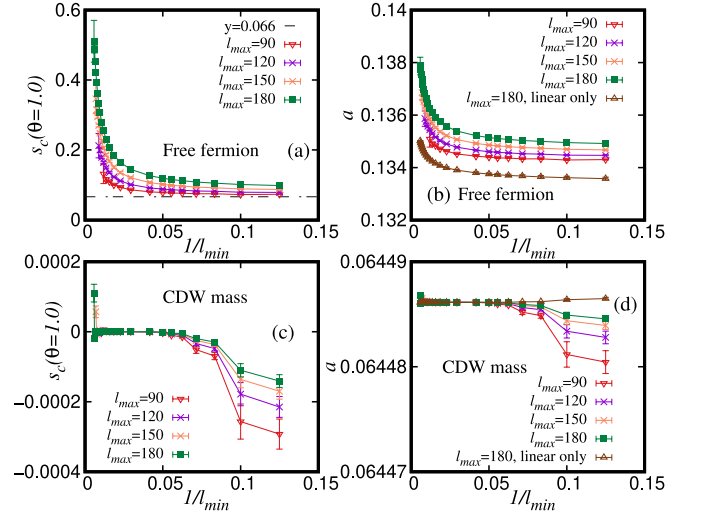


FIG. S4. The fitting range is set by $[l_{min}, l_{max}]$ and the data is fitted to the form $\ln |X(\theta)| = -al + s(\theta) \ln l + c$. Logarithmic coefficient $s(\theta)$ (a) (c) and linear coefficient a (b) (d) as function of the smallest perimeter l_{min} considered in the fitting. We set $L = 90$ and $\theta = 1.0$. (a) and (b) are obtained from the free fermion model and (c) and (d) are obtained from model with CDW mass term. The brown dot lines in (b) and (d) indicate the linear coefficient a extract from the fitting of linear function.

B. RG invariant quantities

As a benchmark to previous calculations [51, 52], we present the RG invariant correlation ratio, $R_c^{\text{QSH/SC}}$ as a function of coupling constant λ in Fig.S5. It is defined as

$$R_c^{\text{QSH/SC}} = 1 - \frac{S_{\text{QSH/U}(1)}(\mathbf{k} = \Gamma + d\mathbf{k}, \tau = 0)}{S_{\text{QSH/U}(1)}(\mathbf{k} = \Gamma, \tau = 0)} \quad (\text{S6})$$

where $d\mathbf{k} = (0, \frac{4\pi}{\sqrt{3}L})$ and $S_{\text{QSH/U}(1)} = \frac{1}{L^2} \sum_{\mathbf{r}, \mathbf{r}'} e^{i\mathbf{q} \cdot (\mathbf{r} - \mathbf{r}')} \text{Tr}\{\hat{O}_{\mathbf{r}} \hat{O}_{\mathbf{r}'}\}$ is the structure factor defined by the order parameter $\hat{O}_{\mathbf{r}}$. The QSH local vector order parameter takes the form of a spin current $\hat{O}_{\mathbf{r}, \delta}^{\text{QSH}} = i\hat{c}_{\mathbf{r}}^\dagger \boldsymbol{\sigma} \hat{c}_{\mathbf{r}+\delta} + \text{H.c.}$ where δ runs over all the next-nearest neighbours of the hexagon labeled by \mathbf{r} . We use the SC local order parameter $\hat{O}_{\mathbf{r}, \delta}^{\text{SC}} = \frac{1}{2} (\hat{c}_{\mathbf{r}+\delta, \uparrow}^\dagger \hat{c}_{\mathbf{r}+\delta, \downarrow}^\dagger + \text{H.c.})$ where δ runs over the sublattice a, b in the honeycomb lattice.

The results for R_c^{QSH} in the vicinity of the GN-QCP are presented in Fig. S5(a). The crossing point of R_c^{QSH} is stable and yields $\lambda_{c1} = 0.0187(2)$. In Fig. S5(b), we observe that R_c^{SC} vanishes upon increasing system size in the vicinity of the GN-QCP. This reflects the absence of the long-range s-wave pairing at this critical point. In Figs. S5(c) and (d), our QMC data suggest that the trends of the crossing points of the two RG invariant quantities R_c^{QSH} and R_c^{SC} converge to the same value as a function of system size. Again, our data is consistent with the estimate $\lambda_{c2} = 0.0332(2)$.

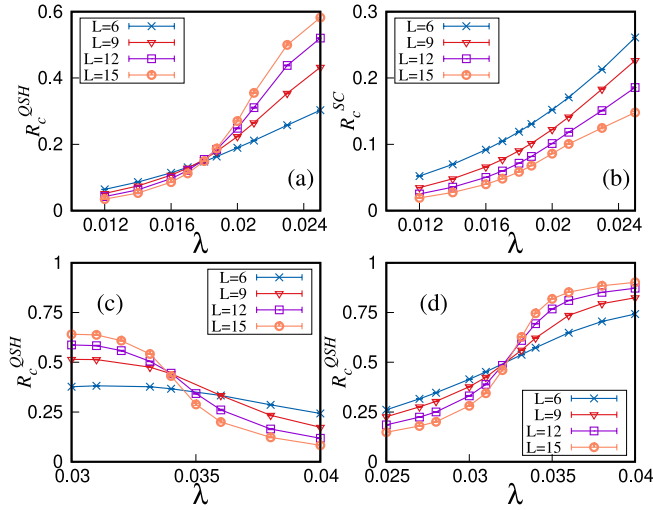


FIG. S5. RG invariant quantities $R_c^{\text{QSH/SC}}$ as function of λ for the model of Eq. (1) in the main text. Due to the expected Lorentz symmetry of the critical points, we scale the inverse temperature with system size: $\beta = 1/T = L$.

TABLE I. Results of coefficient $\alpha(L)$ in thermal dynamic limit by using polynomial fitting in Fig. S9.

$\alpha(L = \infty)$ as function of λ			
Channel	$\lambda = 0.006$	$\lambda_{c1} = 0.01875$	$\lambda_{c2} = 0.03315$
$\alpha_c(\infty)$	0.068(24)	0.044(12)	0.049(17)
$\alpha_s(\infty)$	0.068(31)	0.14(1)	0.12(4)

C. Raw data of disorder operator in the interacting case

In this subsection we show the behavior of the raw data for the disorder operators $X_{c/s}(\theta)$ for various coupling constants λ and rotation angle θ . In Fig. S6, the disorder operator $X_{c/s}(\theta)$ at fixed angle $\theta = \pi/4, \pi/2, 3\pi/4, \pi$ illustrate the evolution as function of coupling λ . Up to $L = 15$, the decay rate of $X_{c/s}(\theta)$ is dominated by the area law $\sim \exp(-aL)$. As we increase the coupling, we observe a clear slowing down of the decay rate.

We now focus on the angle dependence for a given coupling. In Fig. S7, we set the coupling constant to be deep in the three phases and also the vicinity of the two critical points and monitor the trends of $X_{c/s}(\theta)$ as function of θ . On the whole, the decay rate of $X_{c/s}(\theta)$ are also dominated by the area law and increase as the angle grows.

In Fig. S8 we present the analysis of the data carried out so as to extract the logarithmic correction to the area law. As for the mean-field case we define a fit window, and vary the bounds so as to obtain reliable results. Clearly, this is a delicate quantity to extract, but we have found that we obtain consistent results for the fitting range $l_{min} \simeq 10$ and $l_{max} = 40$ for our largest $L = 18$

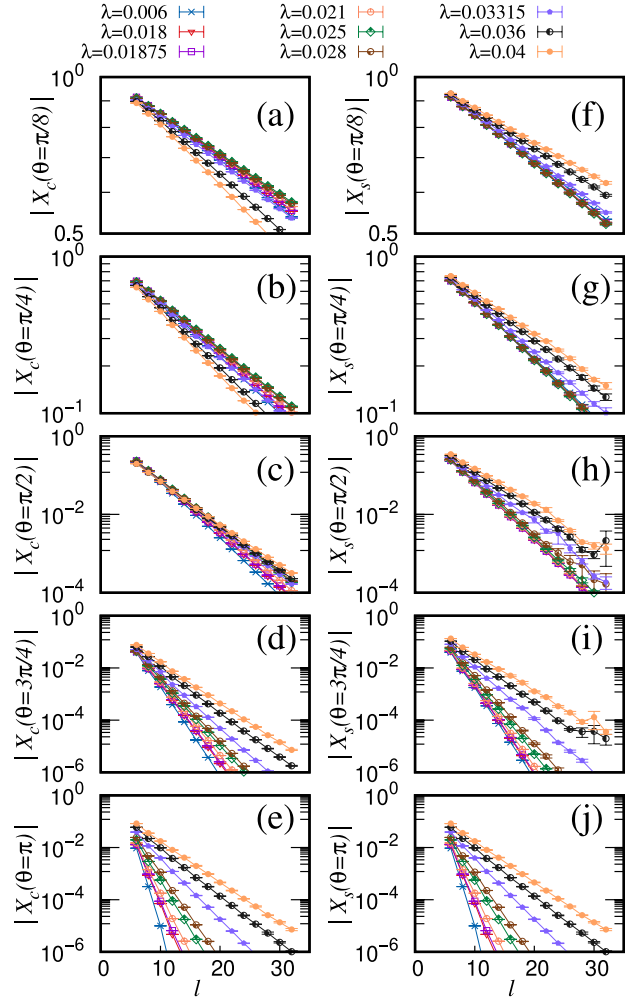


FIG. S6. Disorder operator $X_c(\theta)$ (a)-(e) and $X_s(\theta)$ (f)-(j) obtained from the model of Eq. (1) in the main text as function of perimeter l on the honeycomb lattice. We consider a logarithmic y-axis and $L = \beta = 15$. Different subplots correspond to different rotation angles θ . In each subplot, we present the disorder operator obtained for different λ for comparison.

system. For the results presented in the main text, we choose $l_{max} = 2L+4$ to be the maximum perimeter under periodic boundary condition and $l_{min} = 10$ for $L = 18$ at DQCP and $l_{min} = 8$ for the other parameters.

As supplementary data, we provide the details of the finite size extrapolation analysis of the quadratic coefficients $\alpha_{c/s}(L)$ in different coupling λ . We assume the finite size coefficient obey the power law dependence $\alpha_{c/s}(L) \sim \alpha(\infty) + \kappa L^{-e}$ and using this form in numerical fitting to obtain the true coefficient $\alpha(\infty)$ in the thermodynamic limit. We consider the system size with $L = 6, 9, 12, 15, 18$ and $\beta = L$ scaling in anticipation of $z = 1$. These results are shown in Fig. S9 and Table I.

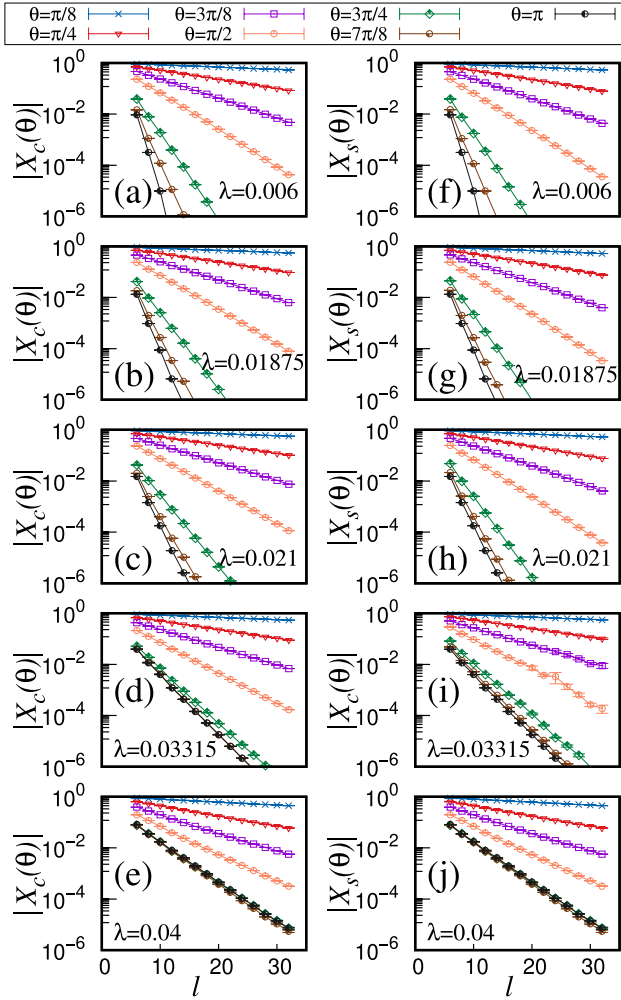


FIG. S7. Disorder operator $X_c(\theta)$ (a)-(e) and $X_s(\theta)$ (f)-(j) obtained for the model of Eq. (1) in the main text as function of perimeter l on the honeycomb lattice. We consider a logarithmic y-axis and $L = \beta = 15$. Different subplots correspond to different coupling constants λ . In each subplot, we present the disorder operator obtained from different rotation angle θ for comparison.

III. π -FLUX MODEL

In this section, we begin with the introduction of the π -flux model. Then we discuss the free case of π -flux model, including the exact expression for the density correlation function, the disorder operator, and compare with the 2d DQCP model, which is defined on the honeycomb lattice. To generalize to the interacting case, we investigate α for the free case, at the GN-Ising QCP so as to obtain an estimate of the current central charge C_J for this QCP.

A. Introduction of π -flux model

To probe a Gross-Neveu Ising transition, from DSM to QSH, we adopt another fermionic model, $H =$

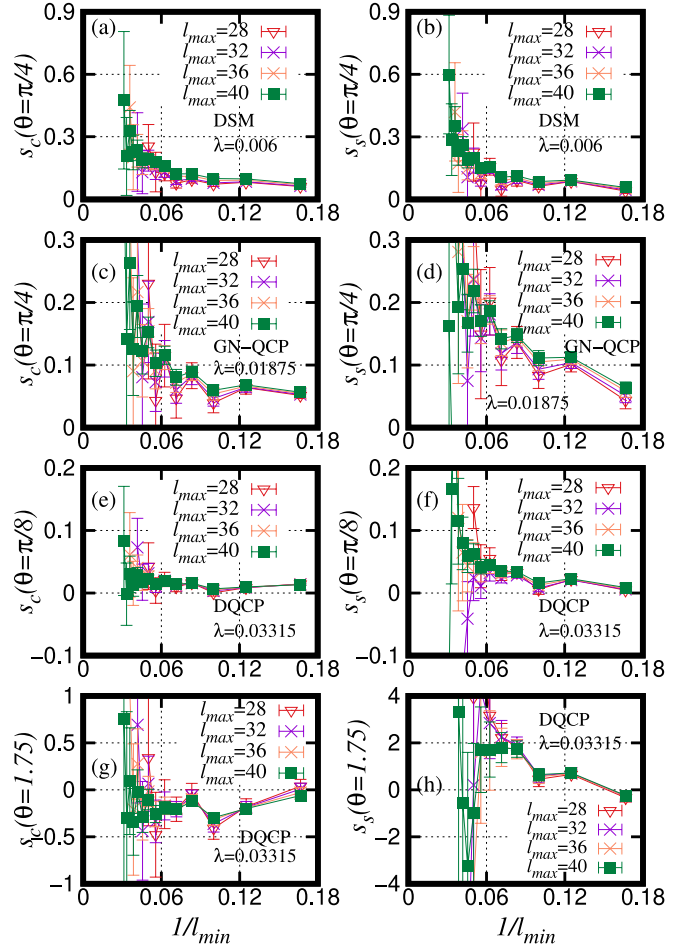


FIG. S8. Logarithmic coefficient $s(\theta)$ as function of smallest perimeter l_{min} consider in fitting. We use the QMC results of $L = \beta = 18$ as the input in numerical fitting.

$H_f + H_{\text{Ising}} + H_{\text{int}}$, defined on the π -flux lattice. The interaction, H_{int} describes the coupling of the free Dirac fermions to a transverse Ising model, H_{Ising} . Specifically,

$$\begin{aligned}
 H_f &= -t \sum_{\langle ij \rangle \sigma} (e^{i\sigma\phi} \hat{c}_{i\sigma}^\dagger \hat{c}_{j\sigma} + e^{-i\sigma\phi} \hat{c}_{j\sigma}^\dagger \hat{c}_{i\sigma}) \\
 H_{\text{Ising}} &= -J \sum_{\langle pq \rangle} \hat{s}_p^z \hat{s}_q^z - h \sum_p \hat{s}_p^x \\
 H_{\text{int}} &= \xi \sum_{\langle\langle ij \rangle\rangle \sigma} \hat{s}_p^z (\hat{c}_{i\sigma}^\dagger \hat{c}_{j\sigma} + \hat{c}_{j\sigma}^\dagger \hat{c}_{i\sigma})
 \end{aligned} \tag{S7}$$

H_f describes the nearest neighbor hopping for fermions, $t = 1$, on the π -flux lattice, $\phi = \frac{\pi}{4}$, and we request spin-up and spin-down fermions to carrier opposite flux patterns to preserve the time-reversal symmetry for the full Hamiltonian. H_{Ising} describes a ferromagnetic $J = 1$ transverse-field Ising model. H_{int} couples the Ising spins with the next nearest neighbor fermion hoppings. The coupling constant $\xi = \pm 1$ has a staggered sign structure alternating between neighboring plaquettes, i.e., $+(-)$

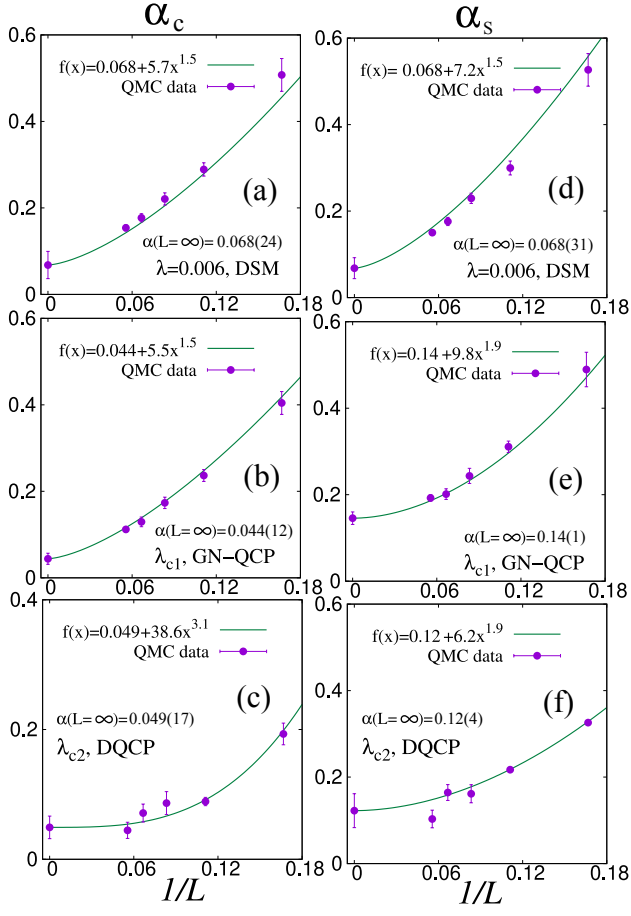


FIG. S9. Coefficient $\alpha_c(L)$ (a)-(c) and $\alpha_s(L)$ (d)-(f) as function of $1/L$ in the QMC simulation. Different subplot correspond to different coupling constants λ . In each subplot we use the power law function $f(x)$ to extract the coefficient $\alpha_{c/s}(L = \infty)$ in thermodynamic limit.

for solid (dashed) bonds as illustrated in Fig. 1(e) in the main text. Tuning the transverse field h the model undergoes a GN-Ising QCP at $h_c = 4.11$ from a DSM phase (at $h < h_c$) and a QSH state (at $h > h_c$). Fig. 1(b), (e) are the corresponding phase diagram and the choice of the entanglement region M .

B. Density correlation function in the free case

Here we investigate another lattice regularization of Dirac fermions, namely the π -flux model. The Hamiltonian reads,

$$\begin{aligned}
 H_f = & -t_1 \sum_{\langle ij \rangle} (e^{i\phi} \hat{c}_i^\dagger \hat{c}_j + e^{-i\phi} \hat{c}_j^\dagger \hat{c}_i) \\
 & -t_2 \sum_{\langle\langle ij \rangle\rangle} (e^{i\phi} \hat{c}_i^\dagger \hat{c}_j + e^{-i\phi} \hat{c}_j^\dagger \hat{c}_i)
 \end{aligned}
 \quad (S8)$$

The sketch of the π -flux model is shown in Fig. 1(e) in the main text. The fermions are located on the lattice

sites, colored in green and blue, indicating two sublattices. \hat{c}^\dagger, \hat{c} are fermion creation and annihilation operators. The fermion hopping term between nearest two green and blue sites has an extra phase factor $e^{i\phi}$, whose sign is positive (negative) along the direction of the arrow. The choice $\phi = \frac{\pi}{4}$ produces a phase π in each plaquette. t_1 represents nearest hopping for different sublattices, while t_2 represents the next-nearest hopping along diagonal lines. The Hamiltonian gives rise to two Dirac cones located at $(0, \pi)$ and $(\pi, 0)$ [53, 54]. As mentioned, we set $t_1 = 1, t_2 = 0$. The low energy physics of the π -flux model is equivalent to that of the honeycomb lattice and, in the absence of spin degree of freedom, is described by two two component Dirac spinors [79]. Furthermore, N_f is directly related to the current central charge in CFT. For single free Dirac fermion, $C_{J,free} = 2$. In the language of lattice model, e.g. both π -flux model, and honeycomb lattice, there are two Dirac points in the Brillouin zone, such that $N_f = 2C_{J,free}$. Note that the Hamiltonian in Eq. (S8) involves spinless fermions. When one considers the limit $\xi = 0$ the two spin flavor decouple, corresponding to $N_f = 8$.

To verify $\alpha = \frac{N_f}{(4\pi)^2}$ at small angle for Dirac cones [63], we calculate the density correlation function in π -flux model,

$$D_\pi(\mathbf{r}) = \langle \hat{n}_{\mathbf{r}_i} \hat{n}_{\mathbf{r}_j} \rangle - \langle \hat{n}_{\mathbf{r}_i} \rangle \langle \hat{n}_{\mathbf{r}_j} \rangle = \frac{N_F}{(4\pi)^2 r^4} \frac{1 - 2 \frac{x y}{r^2} (-1)^{x+y}}{2}
 \quad (S9)$$

where, $\mathbf{r} = \mathbf{r}_i - \mathbf{r}_j$, r is the absolute distance of \mathbf{r} , and $x(y)$ is the component of \mathbf{r} along the $x(y)$ direction. Here corrections to the rotationally invariant IR result are taken into account. To exhibit the above expression in the lattice model, we provide analytic results of the density correlation function in Fig. S10. In lattice models, such as the π -flux model [53, 54], the density correlation function has small variance with respect to Eq. (S9). The red line indicates the $\frac{N_F}{(4\pi)^2 r^4}$ form where $N_F = 4$ for the π -flux model. In Fig. S10 (a), we plot $D(\mathbf{r})$ for each site at $L = 1000, t_1 = 1, t_2 = 0$ and compare with the analytical formula, yellow dots. Differences are apparent at small r , corresponding large momentum, or short wave length contributions. The short wave length properties are determined by the lattice structure or the microscopic interacting coefficients. Next in Fig. S10 (b), we change $t_2 = 0.1$ to verify this difference, where two Dirac cones still remain. We find the difference between yellow and blue dots to be at small r . To further explore the lattice model implementation, we plot the various system size in Fig. S10 (c) and discover when r is comparable with the system size, $D(\mathbf{r})$ will obviously deviate from the $\frac{1}{r^4}$ behavior, which is regarded as a finite system effect. Fig. S10 (d) extracts the lattice sites on the diagonal line, i.e., $x = y$, where the oscillation term in Eq. (S9) gives 1. Here we note that the lattice constant is set to unity such that x and y can be half-integers or integers. The results nicely match with the red line at moderate r for each system size. Thus we conclude that the density

correlation function calculated in the lattice model differs from the continuum limit both at small r and at $r \sim L$, due to lattice microscopic details and finite system sizes, respectively.

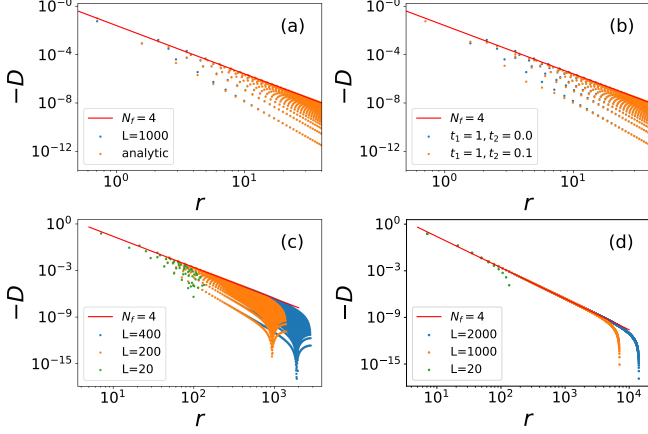


FIG. S10. Analytical density correlation function in Eq. (S9) versus r compared with lattice model results on a ln-ln scale. The red line in each subplots is the same functional form $\frac{N_f}{(4\pi)^2 r^4}$, where $N_f = 4$ for the spinless π -flux model. The points with same color and r represent various values of x, y . (a) $D(r)$ for $L = 1000, t_1 = 1, t_2 = 0$ and dots for Eq. (S9), plotted in blue and yellow. (b) $D(r)$ for $L = 1000, t_1 = 1, t_2 = 0.0$ and $L = 1000, t_1 = 1, t_2 = 0.1$, plotted in blue and yellow. (c) $D(r)$ for $t_1 = 1, t_2 = 0.0$ at various system $L = 400, 200$ and 20 plotted in blue, yellow and green. (d) $D(r)$ for $t_1 = 1, t_2 = 0.0$ at diagonal line, i.e. $x = y$ with various system $L = 2000, 1000$ and 20 plotted in blue, yellow and green.

C. The disorder operator in the free case

Utilizing Eq. (S9), we calculate the disorder operator at small θ in the free case,

$$\frac{\ln(|X(\theta)|)}{\theta^2} = -a_1 l + \frac{N_f}{(4\pi)^2} \ln l + a_0 \quad (\text{S10})$$

The coefficient of area law a_1 is determined by the lattice parameters, e.g., t_1, t_2 . The logarithmic correction is universal, and only depends on N_f . Following, we will focus on the subleading logarithmic correction.

Taking small θ as example, Eq. (S10) is strictly valid only in the limit $L, l \rightarrow \infty$, since one needs to compute the integral over Eq. (S9) in region M , i.e. $\int_{\mathbf{r}_1 \in M} d^2 \mathbf{r}_1 \int_{\mathbf{r}_2 \in M} d^2 \mathbf{r}_2 D_\pi(\mathbf{r}_1 - \mathbf{r}_2)$. Technically, in Monte Carlo simulation for interacting fermionic model, l and L are both finite. Since $\ln l$ is small compared to the leading l term, at finite system size, it is hard to obtain α in the thermodynamic limit by direct fitting for the function form Eq. (1) in the main text at current system size, i.e. $L = 18$ for interacting system. Compared with previous studies on the Bose-Hubbard model, the disorder operator also possess sub-leading $\ln l$ corrections [7]. We

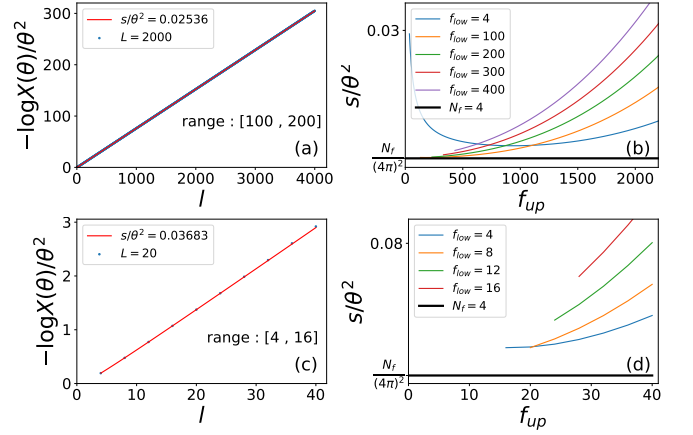


FIG. S11. The scaling behavior of the disorder operator on the π -flux lattice at small angle $\theta = 0.1$ and choice of fitting range for determining coefficient s to show the finite size effect. (a,b) for $L = 2000$, (c,d) for $L = 20$, comparable with the size of the interacting system. (a,c) plots the original disorder operator data versus perimeter l , where $-\ln X$ seems like one linear function. (b,d) show $s(\theta)/\theta^2$ versus various fit range $l \in [f_{low}, f_{up}]$. The analytic value at thermodynamic limit $\frac{N_f}{4\pi^2}$ is plotted by black solid line. We find if the lower boundary f_{low} is too small, as the same order of 1, e.g. the blue line in (b), the fit results will overestimate the value. On the contrast, when the upper boundary f_{up} gets larger, the fit results gradually deviate the analytic value. Thus we conclude the proper choice to get $s(\theta)/\theta^2 = \frac{N_f}{4\pi^2}$ is $1 \ll f_{low} < f_{up} \ll L$. For small size $L = 20$ in (d), we find the condition is hard to satisfy, thus leads to overestimated value for s .

numerically find that the coefficient $-a_1$ of the leading area law term in free Dirac fermions is much larger than that in the Bose-Hubbard model, shown in Fig. S11(a) for $L = 2000$ and (c) for $L = 20$ which leads to difficulties to extract α . Besides, we notice that the choice of the fitting range changes the result, Fig. S11. We denote the fit range as $l \in [f_{low}, f_{up}]$. We plot several choices of f_{low} as curves with various colors, the x-axis being f_{up} . From the above analysis we conclude severe finite size effect for the coefficient.

To obtain α in the thermodynamic limit, we adopt two strategies. In the main text pertaining to interacting systems, we directly fit the log correction for each system size, and then extrapolate to $L \rightarrow \infty$. Both errorbars stemming from the Monte Carlo data as well as the systematic error generated by variation by the choice of the fitting range are taken into account for the estimate of $\alpha(L)$. In contrary to the interacting case, for free systems, we are able to reach large enough lattices so as to approach the thermodynamic limit. By changing the fitting range, we show that one can obtain approximate values of α in the large system size limit. In the following, we will show how to obtain the value, corresponding to $N_f = 4$.

To carry out the analysis, we introduce the concept of so-called optimal fit range. In the finite size, we ob-

serve that all choices of the fitting range will overestimate the log correction as compared to the value in the thermodynamic limit. Therefore for a given system size, we consider the fitting range, which gives the smallest log correction. We find that this smallest log correction will also gradually approach the thermodynamic limit value as L increases.

In Fig. S11 (b) at a large system size, we observe if $1 \ll f_{low} < f_{up} \ll L$ is satisfied, for example $f_{low} = 100, f_{up} = 200$, the fit result $\frac{s}{\theta^2} = 0.02536$ in (a) is close to the analytic value in the continuum limit $\frac{N_f}{(4\pi)^2} = 0.02533$. For comparison, at $L = 20$ in (c,d), we show that whatever the choice of fit range, the result will be larger than $\frac{N_f}{(4\pi)^2}$. Even the optimal fit range $[4, 16]$, corresponding to the closest value to the thermodynamic limit at the considered system size, gives $\frac{s}{\theta^2} = 0.03683$, almost more than one-half the value in the thermodynamic limit. To conclude, we can extract the coefficient as a function of system size $s(\theta, L)$ with the optimal fitting range strategy and then extrapolate to the thermodynamic limit: $\frac{s(\theta \rightarrow 0, L \rightarrow \infty)}{\theta^2} = \frac{N_f}{(4\pi)^2}$. As we showed in Fig. S11, the most optimal value is always the minimum among all possible fit range. This criterion is more unambiguous than above mentioned $1 \ll f_{low} < f_{up} \ll L$. Hence, one may expect $s(\theta, L)$ to gradually approach $s(\theta \rightarrow 0, \infty)$ as L increase.

D. Comparison between the π -flux model and honeycomb lattice implementation

As for the π -flux model, free fermions on the honeycomb lattice form Dirac cones, located at the $(\frac{2\pi}{3}, \frac{2\pi}{3\sqrt{3}})$ and $(-\frac{2\pi}{3}, \frac{2\pi}{3\sqrt{3}})$ points in the Brillouin zone. This corresponds to $C_{J,free} = 2$ and $N_f = 4$. We analytically solve the density correlation function to obtain:

$$D_h(\mathbf{r}) = \langle \hat{n}_{\mathbf{r}_i} \hat{n}_{\mathbf{r}_j} \rangle - \langle \hat{n}_{\mathbf{r}_i} \rangle \langle \hat{n}_{\mathbf{r}_j} \rangle \sim \frac{N_f}{(4\pi)^2 r^4} \quad (\text{S11})$$

$D_h(\mathbf{r})$ has a similar form to $D_\pi(\mathbf{r})$ aside from the oscillation term, shown in Fig. S10, indicating that both have the same scaling behavior of the disorder operator $al + b \ln l + c$ when carrying out the integral over M of the density fluctuations. It must be emphasized that here the region M is a parallelogram, whose degree of corners are $60^\circ, 60^\circ, 120^\circ, 120^\circ$. Here, we use the conclusions in Ref. [58], in which the contribution by corners is described by $s \propto \sum_\alpha f(\alpha) = \sum_\alpha 2(1 + (\pi - \alpha) \cot(\alpha))$, where the summation runs over the interior angle for region M . Thus, we obtain the modification due to the geometry of the parallelogon M -region over the square of $A \approx 1.30$. Hence we have:

$$\frac{\ln(|X(\theta)|)}{\theta^2} = -a_1 l + \frac{AN_f}{(4\pi)^2} \ln l + a_0 \quad (\text{S12})$$

In Fig. S12 we carry out a similar analysis as for the square lattice, Fig. S11. We find $\frac{s(\theta \rightarrow 0, L=24)}{\theta^2} = 0.04065$,

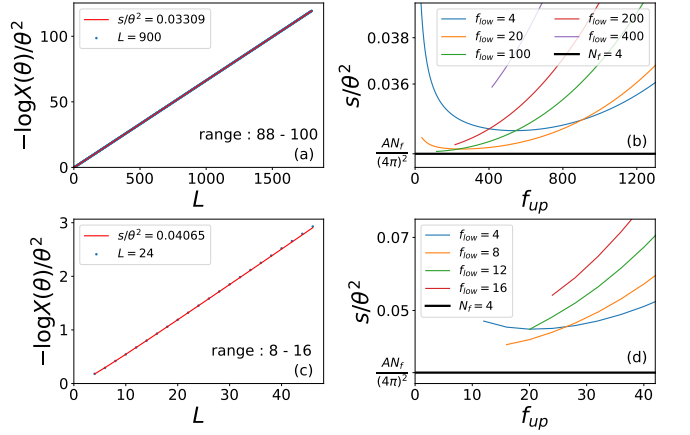


FIG. S12. The scaling behavior of the disorder operator on the honeycomb lattice at small angle $\theta = 0.1$ and choice of fitting range to determine the coefficient s . (a,b) for $L = 900$, (c,d) for $L = 24$, comparable with the size of the interacting system. (a,c) plots the original disorder operator data versus perimeter l , where from $-\ln X$ it seems hard to extract the log correction. (b,d) shows $s(\theta)/\theta^2$ versus f_{up} for various fit ranges $l \in [f_{low}, f_{up}]$. The analytic value in the thermodynamic limit $\frac{N_f}{(4\pi)^2}$ is plotted by a black solid line. We find that if the lower bound f_{low} is too small, blue line in (b), the fit results will overestimate the value. In contrast, when the upper boundary f_{up} gets larger, the fit results gradually deviates from the analytic value. Thus we conclude that the proper choice to obtain $s(\theta)/\theta^2 = \frac{N_f}{(4\pi)^2}$ is for $1 \ll f_{low} < f_{up} \ll L$. For small sizes $L = 24$ in (d), we find the condition is hard to satisfy, thus leading to overestimated values for s .

$\frac{s(\theta \rightarrow 0, L=900)}{\theta^2} = 0.03309$, and $\frac{s(\theta \rightarrow 0, L=24)}{\theta^2} = 0.03299$. The difference for $L = 900$ and $L = 24$ compared with the thermodynamic limit value is 0.3% and 23%.

The result can be applied to 2d DQCP model at $\lambda < \lambda_{c1}$, where one expects in thermodynamic limit with $A \approx 1.3$, $N_f = 8$, $\alpha = \frac{AN_\alpha C_J}{(4\pi)^2} \approx 0.0658$.

E. C_J at Gross-Neveu QCP

In this subsection, we discuss the results at Gross-Neveu QCP, and compare the disorder operator at the Gross-Neveu-Ising and Gross-Neveu-Heisenberg transitions. As mentioned in the main text, the disorder operator at small θ also obeys the expression for Eq. (1) in the main text, where the $\ln l$, coefficient named $s(\theta) \sim \alpha \theta^2$ has the relation with the current central charge C_J in the corresponding CFT. Theoretically, one expects $\alpha = \frac{AN_\alpha C_J}{8\pi^2}$ at the Gross-Neveu QCP, where the angle modification coefficient $A = 1$ for the $(90^\circ, 90^\circ, 90^\circ, 90^\circ)$ square region and $A \approx 1.30$ for $(60^\circ, 60^\circ, 120^\circ, 120^\circ)$ for the parallelogon. We aim to calculate C_J for the Gross-Neveu Ising and Heisenberg QCPs. However, the system size in the interacting case is limited at $L = 20$ for π -flux, and $L = 24$ for honeycomb, leads to the deviation from the analytic value by fitting, as shown in Fig. S11(d) and

Fig. S12(d). That directly indicates that the choice of fit range brings non-negligible influences on the value of α . Besides, the original data of interacting case has errorbars, which differs with the non-interacting case, as shown in Fig. S11 and Fig. S12. Thus, it is difficulty to fit the disorder operator to obtain C_J . Here, based on the knowledge that the disorder operator is the integral over the density correlation function $D(\mathbf{r})$, we directly calculate $D(\mathbf{r})$ by DQMC simulations and compare the result by fitting the disorder operator. We display the calculations in the interacting Hamiltonian in Eq. (S7) in the main text, corresponding to $A = 1$, and Gross-Neveu-Ising universality. Fig. S13 shows the original data for $D(\mathbf{r})$ in a ln-ln scale for our largest system size. At first sight, $D(\mathbf{r})$ at h_c still obeys the $\frac{1}{r^4}$ relation and has a small difference with the free results. To investigate the difference carefully, we plot the ratio between $D(\mathbf{r})$ and $D_{free}(\mathbf{r})$ for various system sizes. At small r , the ratio seems to be independent of L , and gradually decreases. We regard this as the effect on the lattice microscopic details, which is not universal. Conversely, at large r , the ratio which exceeds 1 results from the finite size effect, as r becomes comparable to L . At moderate r , we find a minimum for each L , and we expect that a plateau corresponding to the minimum will appear at large L . We thus plot the so-called extrapolation line in pink and construct the plateau as we expect and finally estimate the value of $\frac{D}{D_{free}} \sim 0.77$ in thermodynamic limit.

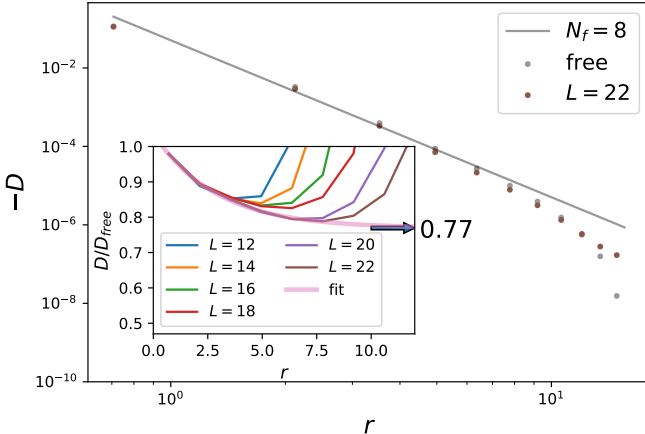


FIG. S13. Density correlation function $D(\mathbf{r})$ versus \mathbf{r} for the Gross-Neveu Ising QCP. We directly plot $D(\mathbf{r})$ along the diagonal for our largest system size, e.g. $\mathbf{r}_x = \mathbf{r}_y$, and compared with the free case D_{free} , plotted in grey on a ln-ln scale. Obviously both follow the $\frac{1}{r^4}$ behavior. The difference in such scale is small and hard to distinguish. To obtain C_J , $\frac{D}{D_{free}}$ is displayed in the inset for various values of L . We expect at $1 \ll r \ll L$, $\frac{D}{D_{free}}$ to converge to the thermodynamic limit. Limited by the system size, we use the grey thick line to depict the extrapolated value with respect the existing data. We fit for several data points along the envelop with the form, $y = c + ae^{-bx}$. We estimate $\frac{D}{D_{free}} \equiv c \sim 0.77$ in the thermodynamic limit.

IV. 1D DQCP MODEL

In this section, we provide data on the convergence check of DMRG simulations.

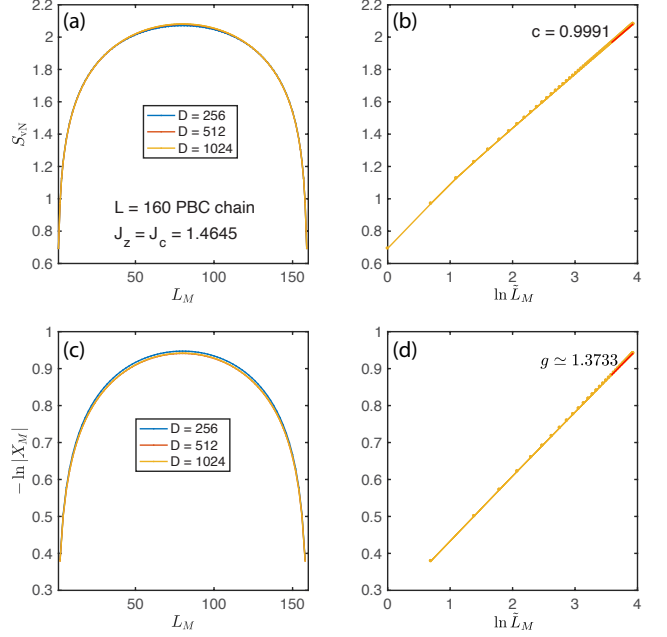


FIG. S14. We consider the $L = 160$ 1D DQCP model at the DQCP point $J_z = J_c = 1.4645$ with periodic boundary condition (PBC). (a, b) shows the entanglement (von Neumann) entropy S_{vN} and (c, d) the logarithmic disorder operator $-\ln |X_M|$ for the DMRG ground states at different bond dimensions $D = 256, 512, 1024$. L_M corresponds to the subsystem size and $\tilde{L}_M = \frac{L}{\pi} \sin \frac{\pi L_M}{L}$ is the conformal distance. Here, the color code for different bond dimension D as indicated in both the panel (a) and (c). From (b) and (d), the central charge $c = 0.9991$ and Luttinger parameter $g = 1.3733$ are extracted from the rather straight line composed by the largest 40 data (as indicated by the red solid line).

Throughout our DMRG simulations for different system size $L = 64, 96, 128, 160$, we keep up to 1024 bond states, which render a small truncation error of $\delta\rho < 5 \times 10^{-9}$. In this section, we show that for our largest system size $L = 160$ and at the critical point $J_z = J_c = 1.4645$, the data presented in the main text is well converged.

In Fig. S14 (a) and (b), we show the entanglement (von Neumann) entropy $S_{vN} = -\text{tr}(\rho_M \ln \rho_M)$ as functions of subsystem size L_M and the corresponding conformal distance $\tilde{L}_M = \frac{L}{\pi} \sin \frac{\pi L_M}{L}$. Here $\rho_M = \text{tr}_M |\psi\rangle\langle\psi|$ is the reduced density matrix obtained by tracing out the degrees of freedom in subsystem M . From panel (a) we can see that, S_{vN} is well converged for $D \geq 512$. We then plot the $D = 1024$ data versus the logarithmic conformal distance $\ln \tilde{L}_M$ following the expected CFT behaviour $S_{vN} = \frac{c}{3} \ln \tilde{L}_M$, from which $c = 0.9991$ is extracted.

For the disorder operator $X_M = \prod_{i \in M} \sigma_i^z$, we repeat the similar analysis in Fig. S14(c) and (d). Again, the

logarithmic disorder operator $-\ln |X_M|$ is well converged for $D \geq 512$. From $-\ln |X_M| = \frac{g}{8} \ln \tilde{L}_M$, $g = 1.3733$ is extracted at the 1D DQCP point.